Research article

Rupesh Ghimire*, Jhih-Sheng Wu*, Vadym Apalkov* and Mark I. Stockman*

Topological nanospaser

https://doi.org/10.1515/nanoph-2019-0496
Received December 5, 2019; revised February 11, 2020; accepted February 12, 2020

Abstract: We propose a nanospaser made of an achiral plasmonic–metal nanodisk and a two-dimensional chiral gain medium – a monolayer nanoflake of a transition-metal dichalcogenide (TMDC). When one valley of the TMDC is selectively pumped (e.g. by a circular-polarized radiation), the spaser (surface plasmon amplification by stimulated emission of radiation) generates a mode carrying a topological chiral charge that matches that of the gain valley. There is another, chirally mismatched, time-reversed mode with exactly the same frequency but the opposite topological charge; it is actively suppressed by the gain saturation and never generates, leading to a strong topological protection for the generating matched mode. This topological spaser is promising for use in nano-optics and nanospectroscopy in the near field especially in applications to biomolecules that are typically chiral. Another potential application is a chiral nanolabel for biomedical applications emitting in the far field an intense circularly polarized coherent radiation.

Keywords: near-field optics; spaser; optical pumping; plasmonics; symmetry protected topological states; topological materials; valleytronics.

1 Introduction

Spaser (surface plasmon amplification by stimulated emission of radiation) was originally introduced in 2003 as a nanoscopic phenomenon and device: a generator and amplifier of coherent nanolocalized optical fields. Since then, the science and technology of spasers experienced a rapid progress. Theoretical developments [1–4] were followed by the first experimental observations of the spaser [5, 6] and then by an avalanche of new developments, designs, and applications. Currently, there are spasers whose generation spans the entire optical spectrum, from the near-infrared to the near-ultraviolet [7–15].

Several types of spasers, which are synonymously called also nanolasers, have so far been well developed. Historically, the first is a nanoshell spaser [5] that contains a metal nanosphere as the plasmonic core that is surrounded by a dielectric shell containing gain material, typically dye molecules [5, 16]. Such spasers are the smallest coherent generators produced so far, with sizes on the order of 10 nm. Almost simultaneously, another type of nanolasers was demonstrated [6] that was built from a semiconductor gain nanorod situated over a surface of a plasmonic metal. It has a micrometer-scale size along the nanorod. Its modes are surface plasmon (SP) polaritons with nanometer-scale transverse size. Given that the spasers of this type are relatively efficient sources of far-field light, they are traditionally called *nanolasers*, although an appropriate name would be *polaritonic spasers*. Later, this type of nanolasers (polaritonic spasers) was widely developed and perfected [7, 12, 17–20]. There are also spasers that are similar in design to the polaritonic nanolasers but are true nanospasers whose dimensions are all on the nanoscale. Such a spaser consists of a monocrystal nanorod of a semiconductor gain material deposited atop of a monocrystal nanofilm of a plasmonic metal [21]. These spasers possess very low thresholds and are tunable in all visible spectra by changing the gain semiconductor composition, while the geometry remains fixed [11, 14, 22]. There are also other types of demonstrated spasers. Among them, we mention semiconductor-metal nanolasers [23] and polaritonic spasers with plasmonic cavities and quantum dot gain media [24].

A fundamentally different type of quantum generators is the lasing spaser [4, 25, 26]. A lasing spaser is a periodic array of individual spasers that interact in the near field and form a coherent collective mode. Such lasing spasers have been built of plasmonic crystals that incorporate gain media. One type of lasing spasers is a periodic array of holes in a plasmonic metal film deposited on a semiconductor gain medium [10]; another type

***Corresponding authors: Rupesh Ghimire, Jhih-Sheng Wu, Vadym Apalkov and Mark I. Stockman,** Center for Nano-Optics (CeNO) and Department of Physics and Astronomy, Georgia State University, Atlanta, GA 30303, USA, e-mail: rghimire1@student.gsu.edu. https://orcid.org/0000-0001-5729-6402 (R. Ghimire); b91202047@gmail.com (J.-S. Wu); vapalkov@gsu.edu (V. Apalkov); mstockman@gsu.edu. https://orcid.org/0000-0002-6996-0806 (M.I. Stockman)

is a periodic array of metal nanoparticles surrounded by a dye molecules solution [27]. We have recently proposed a topological lasing spaser that is built of a honeycomb plasmonic crystal of silver nanoshells containing a gain medium inside [28]. The generating modes of such a spaser are chiral SPs with topological charges of $m = \pm 1$, which topologically protects them against mixing. Only one of the $m = \pm 1$ topologically charged modes can generate at a time selected by a spontaneous breaking of the time-reversal ($\mathcal{T}$) symmetry.

The spasers not only are of a significant fundamental interest but also are promising for applications based on their nanoscale-size modes and high local fields. Among such demonstrated applications are those to sensing of minute amounts of chemical and biological agents in the environment [18, 19, 29]. Another class of the demonstrated applications of the spasers is that in cancer theranostics (therapeutics and diagnostics) [16]. An important perspective application of spasers is on-chip communications in optoelectronic information processing [30].

It is of a great interest to explore intersections of the spaser technology and topological physics. In our recently proposed topological lasing spaser [28], the topologically charged eigenmodes stem from the Berry curvature [31, 32] of the plasmonic Bloch bands of a honeycomb plasmonic crystal of silver nanoshells. In contrast, the gain medium inside these nanoshells is completely achiral. This topological lasing spaser is predicted to generate a pair of mutually time-reversed eigenmodes carrying topological charges of ±1, which strongly compete with each other, so only one of them can be generated at a time.

Topology plays an important role in all fields of physics, from condensed matter physics to cosmology. In solids, the topological properties are determined by the change of the phase of an electron wave function and are quantified by the Berry connection and the corresponding Berry curvature. The Berry curvature acts as a magnetic field in the reciprocal space, and the flux of the Berry curvature through the first Brillouin zone determines the total topological charge that is quantized and is called the Chern number.

Although for the systems with the $\mathcal{T}$ symmetry the total topological charge is zero, it can have nonzero values and even quantized within some regions of the reciprocal space called *valleys*. An example of such systems is graphene, which is semimetal with two inequivalent points, K and K', in the reciprocal space, where the electron energy dispersion is of a relativistic Dirac type. The Berry curvature at these two points is singular and zero elsewhere. The total flux of the Berry curvature through any surface that encloses K or K' point is quantized topological charge, which is (in units of π) 1 at the K point and –1 at the K' point. The corresponding electron states at these two points are chiral, as completely determined by their topology, with opposite chiralities, which is protected by the $\mathcal{T}$ symmetry.

While for the gapless graphene the topological charge at the K or K' point is quantized, in two-dimensional semiconductors such as transition-metal dichalcogenide (TMDC) materials, which have the same honeycomb crystal structure as graphene but broken inversion symmetry and, consequently, a finite bandgap, there is no quantization of the topological charges at the two valleys, K or K'. In the TMDCs, the Berry curvature has a maximum at the K points, but it is not singular. It monotonically decreases away from the K points, and the corresponding Berry flux is nonuniversal and, by modulus (in units of π), is always less than 1. Despite this, the chiral nature of the electron states at the K points is preserved. Namely, the state are chiral with opposite chiralities at two valleys, K and K', as protected by $\mathcal{T}$-reversal symmetry. This property is crucial for our analysis below, where the interaction of the TMDC material with plasmon modes is considered.

In this article, we propose a topological nanospaser that also generates a pair of mutually time-reversed chiral SP eigenmodes with topological charges of ±1, whose fields are rotating in time in the opposite directions. In a contrast to the findings of Wu et al. [28], this proposed spaser is truly nanoscopic, with a radius ~10 nm. The topological charges (chiralities) of its eigenmodes originate from the Berry curvature of the gain-medium Bloch bands. This gain medium is a two-dimensional honeycomb nanocrystal of a TMDC [33–35]. The plasmonic subsystem is an achiral nanodisk of a plasmonic metal. Note that previously the TMDCs have been used as the gain media of microlasers where the cavities were formed by microdisk resonators [36, 37] or a photonic crystal microcavity [38]. None of these lasers generated a chiral, topologically charged mode.

2 Spaser structure and main equations

The geometry and the fundamentals of functioning of the proposed topological nanospaser are illustrated in Figure 1. This spaser consists of a thin silver nanospheroid placed atop of the two-dimensional gain medium (a nanodisk of a monolayer TMDC) (Figure 1A). As Figure 1B illustrates, the gain medium is pumped with circularly polarized light, which is known to selectively

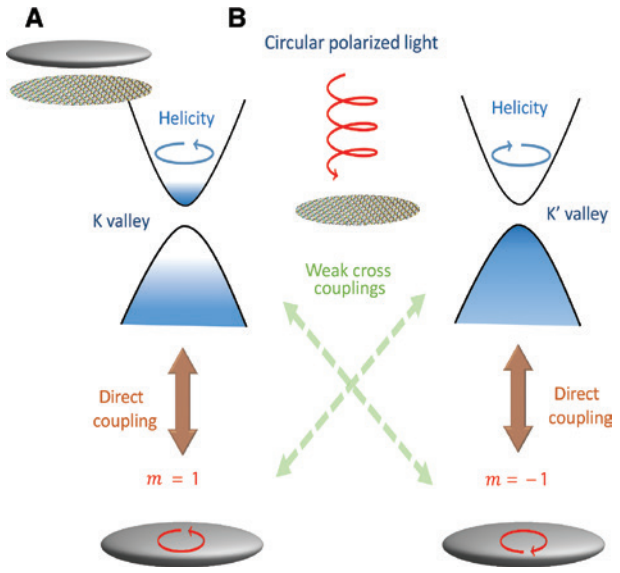

Figure 1: Schematic of the spaser geometry and operation. (A) Geometry of the spaser: silver nanospheroid on TMDC. (B) Schematic of spaser operation. Pumping with a circular-polarized light excites the valley whose chirality is matched to the light helicity. The stimulated VB → CB transitions at the corresponding *K* or *K*′ point excite SPs matched by chirality to that of the valley; the other, mismatched valley couples only weakly to these SPs.

populate one of the *K* or *K*′ valleys, depending on its helicity [39, 40]. Because of the axial symmetry, the plasmonic eigenmodes, $\phi(\mathbf{r})$, depend on the azimuthal angle, φ: $\phi_m(\mathbf{r}) \propto \exp(im\varphi)$, where $m = \text{const}$ is the magnetic quantum number. Figure 1B illustrates that the conduction band (CB) to valence band (VB) transitions in the TMDC couple predominantly to the SPs whose chirality matches that of the valley: the transitions in *K* or *K*′ valley excite the $m = 1$ or $m = -1$ SPs, respectively.

The SP eigenmodes $\phi_n(\mathbf{r})$ are described by the quasistatic equation:

$$\nabla\Theta(\mathbf{r})\nabla\phi_n(\mathbf{r}) = s_n\nabla^2\phi_n(\mathbf{r}), \tag{1}$$

where n is a set of the quantum numbers defining the eigenmode; s_n is the corresponding eigenvalue, which is a real number between 0 and 1; and $\Theta(\mathbf{r})$ is the characteristic function, which is equal to 1 inside the metal and 0 outside. We assume that the metal nanoparticle is a spheroid whose eigenmodes can be found in oblate spheroidal coordinates (see Supplementary Materials). They are characterized by two-integer spheroidal quantum numbers: multipolarity $l = 1, 2, \ldots$ and azimuthal or magnetic quantum number $m = 0, \pm1, \ldots$. We will consider a dipolar mode, $l = 1$, where $m = 0, \pm1$. Note that the dipole transitions in the TMDC at the *K*, *K*′ points are chiral, and they couple only to the modes with $m = \pm1$. The Hamiltonian of the SPs is

$$H_{\text{SP}} = \hbar\omega_{\text{sp}}\sum_{m=\pm1}\hat{a}_m^\dagger\hat{a}_m, \tag{2}$$

where ω_{sp} is the SP frequency, and $\hat{a}_m^\dagger$ and $\hat{a}_m$ are the SP creation and annihilation operators (we indicate only the magnetic quantum number m). The electric field operator is

$$\mathbf{F}_m(\mathbf{r}, t) = -A_{\text{sp}}\nabla\phi_m(\mathbf{r})(\hat{a}_m e^{-i\omega_{\text{sp}}t} + \hat{a}_m^\dagger e^{i\omega_{\text{sp}}t}), \tag{3}$$

$$A_{\text{sp}} = \sqrt{\frac{4\pi\hbar s_{\text{sp}}}{\varepsilon_d s'_{\text{sp}}}}, \tag{4}$$

where $s'_{\text{sp}} = \text{Re}\left[ds(\omega)/d\omega|_{\omega=\omega_{\text{sp}}}\right]$. The monolayer TMDC is coupled to the field of the SPs via the dipole interaction. We choose the proper thickness of the silver spheroid so that the SP energy $\hbar\omega_{\text{sp}}$ is equal to the bandgap of the TMDC gain medium. The Hamiltonian of the TMDC near the *K* or *K*′ point can be written as

$$H_{\mathcal{K}} = \int d^2\mathbf{q}\sum_{\alpha=\text{v,c}} E_\alpha(\mathcal{K}+\mathbf{q})|\alpha, \mathcal{K}+\mathbf{q}\rangle\langle\alpha, \mathcal{K}+\mathbf{q}|, \tag{5}$$

where $\mathcal{K} = K$ or *K*′, and v and c stand for the VB and the CB, correspondingly. We expand the Hamiltonian around the *K* and *K*′ points as

$$H_{\mathcal{K}} \simeq \nu_{\mathcal{K}}\sum_{\alpha=c,v} E_\alpha(\mathcal{K})|\alpha, \mathcal{K}\rangle\langle\alpha, \mathcal{K}|, \tag{6}$$

where $\nu_{\mathcal{K}}$ is the density of electronic states in the $\mathcal{K}$ valley, which we adopt from experimental data [36, 41]: $\nu_{\mathbf{K}} = \nu_{\mathbf{K}'} = 7.0\times10^{12}\ \text{cm}^{-2}$.

The field of the SPs in nanoparticles is highly nonuniform in space, which gives rise to a spatial nonuniformity of the electron population of the TMDC monolayer. To treat this, we employ a semiclassical approach where the state $|\alpha, \mathcal{K}, \mathbf{r}\rangle$ represents an electron in the $\mathcal{K}$ valley at position $\mathbf{r}$. The corresponding Hamiltonian in the semiclassical approximation can be written as

$$H_{\mathcal{K}} = \nu_{\mathcal{K}}\sum_{\alpha=c,v} E_\alpha(\mathcal{K})\int d^2\mathbf{r}|\alpha, \mathcal{K}, \mathbf{r}\rangle\langle\alpha, \mathcal{K}, \mathbf{r}| \tag{7}$$

The interaction between the monolayer TMDC and the SPs is described by an interaction Hamiltonian

$$H_{\text{int}} = -\nu_{\mathbf{K}}\sum_{\mathcal{K}=\mathbf{K},\mathbf{K}'}\int d^2\mathbf{r}\sum_{m=\pm1}\mathbf{F}_m(\mathbf{r})\hat{\mathbf{d}}_{\mathcal{K}}(\mathbf{r}), \tag{8}$$

where the dipole operator is given by

$$\hat{\mathbf{d}}_{\mathcal{K}}(\mathbf{r}) = \mathbf{d}_{\mathcal{K}} e^{i\Delta_g t} |c, \mathcal{K}, \mathbf{r}\rangle\langle v, \mathcal{K}, \mathbf{r}| + \text{h.c.}, \tag{9}$$

and $\hbar\Delta_g$ is the bandgap (at the K or K' point).

The transition dipole element, $\mathbf{d}_{\mathcal{K}}$, is related to the non-Abelian (interband) Berry connection $\mathcal{A}^{(cv)}(\mathbf{k})$ as

$$\mathbf{d}_{\mathcal{K}} = e\mathcal{A}^{(cv)}(\mathbf{k}),$$
$$\mathcal{A}^{(cv)}(\mathbf{k}) = i\left\langle u_{c\mathbf{k}} \left| \frac{\partial}{\partial \mathbf{k}} \right| u_{v\mathbf{k}} \right\rangle \Big|_{\mathbf{k}=\mathcal{K}}, \tag{10}$$

where $u_{\alpha\mathbf{k}}$ is the normalized lattice-periodic Bloch function.

In this article, we consider the dynamics of the system semiclassically; we treat the SP annihilation and creation operators as complex c numbers, $\hat{a}_m = a_m$ and $\hat{a}_m^\dagger = a_m^*$, and describe the electron dynamics quantum mechanically by density matrix $\hat{\rho}_{\mathcal{K}}(\mathbf{r}, t)$. Furthermore, we assume that the SP field amplitude is not too large, $\tilde{\Omega}_{m,\mathcal{K}} \ll \Delta_g$, where the Rabi frequency is defined by

$$\tilde{\Omega}_{m,\mathcal{K}}(\mathbf{r}) = -\frac{1}{\hbar} A_{sp} \nabla\phi_m(\mathbf{r}) \mathbf{d}_{\mathcal{K}}^*. \tag{11}$$

Then we can employ the rotating wave approximation [42, 43], where the density matrix can be written as

$$\hat{\rho}_{\mathcal{K}}(\mathbf{r}, t) = \begin{pmatrix} \rho_{\mathcal{K}}^{(c)}(\mathbf{r}, t) & \rho_{\mathcal{K}}(\mathbf{r}, t) e^{i\omega t} \\ \rho_{\mathcal{K}}^*(\mathbf{r}, t) e^{-i\omega t} & \rho_{\mathcal{K}}^{(v)}(\mathbf{r}, t) \end{pmatrix}. \tag{12}$$

Following Stockman, the equations of motion of the SPs and the monolayer TMDC electron density matrix are

$$\dot{a}_m = [i(\omega - \omega_{sp}) - \gamma_{sp}] a_m + i\nu_{\mathcal{K}} \int_S d^2\mathbf{r} \sum_{\mathcal{K}} \rho_{\mathcal{K}}^*(\mathbf{r}) \tilde{\Omega}_{m,\mathcal{K}}^*(\mathbf{r}), \tag{13}$$

$$\dot{n}_{\mathcal{K}}(\mathbf{r}) = -4 \sum_{m=1,-1} \mathrm{Im}\left[\rho_{\mathcal{K}}(\mathbf{r}) \tilde{\Omega}_{m,\mathcal{K}}(\mathbf{r}) a_m\right] + g_{\mathcal{K}}\left[1 - n_{\mathcal{K}}(\mathbf{r})\right] - \gamma_{2\mathcal{K}}(\mathbf{r})\left[1 + n_{\mathcal{K}}(\mathbf{r})\right], \tag{14}$$

$$\dot{\rho}_{\mathcal{K}}(\mathbf{r}) = [-i(\omega - \Delta_g) - \Gamma_{12}] \rho_{\mathcal{K}}(\mathbf{r}) + i n_{\mathcal{K}}(\mathbf{r}) \sum_{m=1,-1} \tilde{\Omega}_{m,\mathcal{K}}^* a_m^*, \tag{15}$$

where S is the entire area of the TMDC, γ_{sp} is the SP relaxation rate, Γ_{12} is the polarization relaxation rate for the spasing transition $2 \to 1$, and $g_{\mathcal{K}}$ is the pumping rate in valley $\mathcal{K}$; the population inversion, $n_{\mathcal{K}}$, is defined as

$$n_{\mathcal{K}} \equiv \rho_{\mathcal{K}}^{(c)} - \rho_{\mathcal{K}}^{(v)}, \tag{16}$$

and the spontaneous emission rate of the SPs is

$$\gamma_{2\mathcal{K}}(\mathbf{r}) = \frac{2(\gamma_{sp} + \Gamma_{12})}{(\omega_{sp} - \Delta_g)^2 + (\gamma_{sp} + \Gamma_{12})^2} \sum_{m=1,-1} |\tilde{\Omega}_{m,\mathcal{K}}(\mathbf{r})|^2. \tag{17}$$

3 Results and discussion

3.1 Parameters of spaser and chiral coupling to gain medium

We consider a spaser consisting of an oblate silver spheroid with semimajor axis $a = 12$ nm placed atop of a circular TMDC flake of the same radius. We assume that the system is embedded into a dielectric matrix with permittivity $\varepsilon_d = 2$. We choose the value of the semiminor axis c (the height of the silver spheroid) to fit ω_{sp} to the K point CV $\to$ VB transition frequency in the TMDC, $\omega_{sp} = \Delta_g$. We employ the three-band tight-binding model for monolayers of group-VIB TMDCs of Liu et al. [44]. We also set $\hbar\Gamma_{12} = 10$ meV.

From the tight-binding model, we calculate the band structure, including bandgap Δ_g and the transition dipole matrix element $\mathbf{d}$. Note that at the K and K' points the bandgaps are the same, $\Delta_g(\mathbf{K}) = \Delta_g(\mathbf{K}')$, while the transition dipole matrix elements are complex conjugated, $\mathbf{d}_{\mathbf{K}} = \mathbf{d}_{\mathbf{K}'}^*$, as protected by the $\mathcal{T}$ symmetry. The values used in the computations are listed in Supplementary Materials. Here we give an example for MoS_2: $c = 1.2$ nm; $\hbar\Delta_g = 1.66$ eV; $\mathbf{d}_{\mathbf{K}} = 17.7\,\mathbf{e}_+$ D, and $\mathbf{d}_{\mathbf{K}'} = 17.7\,\mathbf{e}_-$ D, where $\mathbf{e}_\pm = (\mathbf{e}_x \pm i\mathbf{e}_y)/\sqrt{2}$ are the chiral unit vectors.

A fundamental question regarding any spaser is the existence of a finite spasing threshold. There are two modes with the opposite chiralities, $m = \pm 1$, and identical frequencies, ω_{sp}, which are time-reversed with respect to each other, whose wave functions are $\nabla\phi \propto e^{\pm i\varphi}$. In the center of the TMDC patch, i.e. at $\mathbf{r} = 0$, the point symmetry group of a metal nanospheroid on the TMDC is C_{3v}. It contains a C_3 symmetry operation, i.e. a rotation in the TMDC plane by an angle $\varphi = \pm 2\pi/3$, which brings about a chiral selection rule $m = 1$ for the K point and $m = -1$ for the K' point, i.e. the chirality of the SPs matches that of the valley. For eccentric positions, which are not too far from $\mathbf{r} = 0$, this selection rule is not exact, but still there is a preference for the chirally matched SPs.

We assume that the pumping is performed with the circularly polarized radiation, and one of the valleys, say the K

valley, is predominantly populated. Consequently, the first mode that can go into generation is the $m=1$ SP. To find the necessary condition that the corresponding threshold can be achieved, we will follow Stockman and set $n_{\mathcal{K}}=1$. Then from (13) and (15), we obtain this condition as

$$\nu_{\mathbf{K}}\int_S \left|I_m^{(\pm)}(\mathbf{r})\right|^2 \mathrm{d}^2\mathbf{r}\geq 1, \tag{18}$$

where ± is the chirality of the pumped TMDC valley, and the coupling amplitude is

$$I_m^{(\pm)}(\mathbf{r})=\frac{\tilde{\Omega}_{m,\mathcal{K}}}{\sqrt{\gamma_{\mathrm{sp}}\Gamma_{12}}}=\frac{A_m d_{\mathcal{K}}}{\hbar\sqrt{\gamma_{\mathrm{sp}}\Gamma_{12}}}\nabla\phi_m(\mathbf{r})\mathbf{e}_{\pm}. \tag{19}$$

Note that $I_m^{(\pm)*}=I_{-m}^{(\mp)}$.

This coupling amplitude is illustrated in Figure 2 for $I_m^{(+)}$. As we see, for the chiral-matched SP with $m=1$, the coupling amplitude is approximately constant, $I_m^{(+)}\approx 1$ within the geometric footprint of the silver spheroid, which is seen in Figure 2A as an almost uniform orange disk with radius $a=12$ nm. In sharp contrast, the chiral-mismatched mode with $m=-1$ (Figure 2B) has virtually no coupling to the TMDC transitions in the K valley, which means that only for one mode the transition dipole matrix element and the corresponding Rabi frequency are large. This property illustrates selectivity of the coupling of electronic states in TMDC and plasmonic modes in nanospheroid. Thus, for the gain medium whose radius R_g is within the footprint of the metal spheroid, i.e. for $R_g\leq a$, only one mode with chirality $m=1$ will be generated. However, for a larger gain medium, $R_g\geq 13$ nm, there is a circle of strong coupling of the mismatched mode, which can potentially go into the generation.

3.2 Kinetics of continuous-wave spasing

Below in this article, we provide numerical examples of the spaser kinetics. For certainty, we assume that the K valley is selectively pumped, which can be done with the right-hand circularly polarized pump radiation. (As protected by the $\mathcal{T}$ symmetry, exactly the same results are valid for the left-handed pump and the K' valley.) Thus, we set $g_K=g$ and $g_{K'}=0$.

A continuous-wave solution can be obtained by solving (13–15), where the time derivatives in the left-hand sides are set to zero. The calculated dependences of the generated coherent SP population, $N_m=|a_m|^2$ where $m=\pm 1$, on the pumping rate, g, for various TMDCs are shown in Figure 3A. As we can see, there is a single spasing threshold for each of the TMDCs. Significantly above the threshold, for $g_{\mathcal{K}}>30\,\mathrm{ps}^{-1}$, the number of SPs, N_m, grows linearly with pumping rate g. This is a common general property of all spasers; it stems from the fact that the feedback in the spasers is very strong due to the extremely small modal volume. Therefore, the stimulated emission dominates the electronic transitions between the spasing levels, which is a prerequisite of the linear dependence $N_m(g)$. The slope of this straight line (the so-called slope efficiency) is specific for every given TMDC. For all these spasers, the threshold condition of (18) for the generation of the matched mode is satisfied. We have verified that the mismatched mode ($m=-1$) does not have a finite threshold; i.e. it is not generated at any pumping rate. The reason is that the matched mode ($m=1$) above its threshold clamps the inversion at a constant level, preventing its increase with the pumping and thus precluding the generation of the mismatched mode.

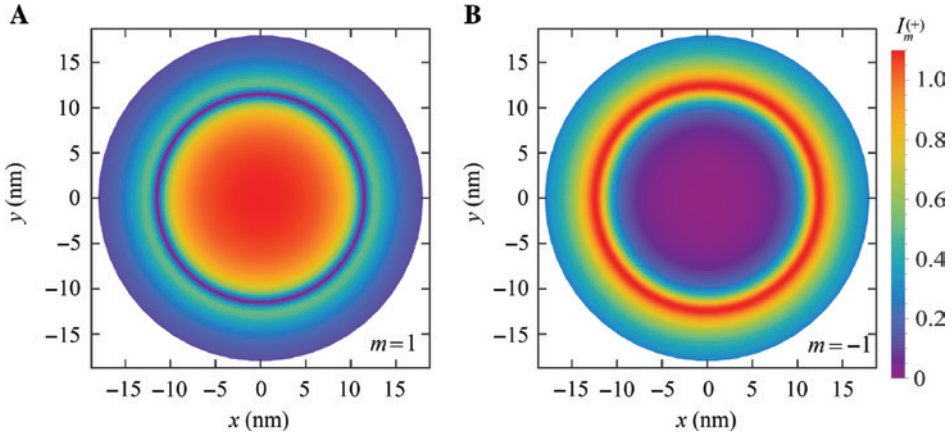

Figure 2: Coupling amplitude between SPs and TMDC dipole transitions is shown for different modes m.
(A) $m=+1$ and (B) $m=-1$. The magnitude is color coded by the bar to the right. The radius of the metal spheroid is $a=12$ nm.

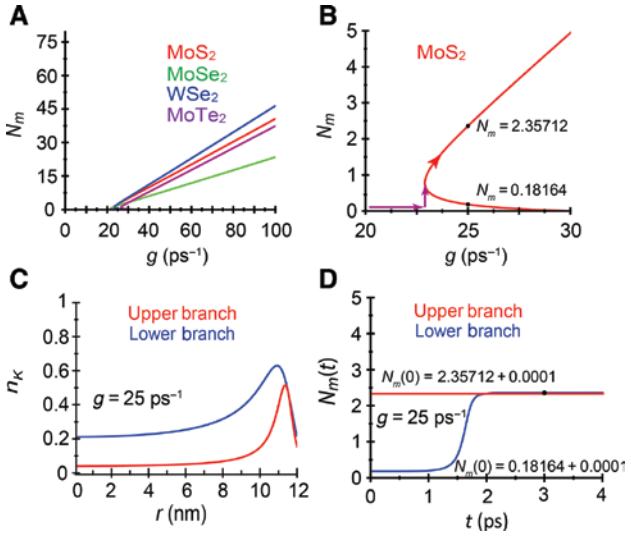

Figure 3: Spaser kinetics.
(A) Dependence of the number of SP quanta in the spasing mode on the pumping rate for gain medium of the matched radius, $R_g = a = 12$ nm. Only the chirality-matched SPs with $m = 1$ are generated. (B) Magnified near-threshold portion of panel (A) for MoS_2. The number of SPs, N_m, is indicated for the points shown on the graphs for the two branches. (C) Radial distribution of the inversion, n_k, for each of the two branches. (D) Test of stability of the two SP branches. The kinetics of the SP population, N_m, after the number of the SPs in each branch is increased by $\Delta N_m = 0.0001$.

In this case, the single chiral mode generation enjoys a strong topological protection.

At the threshold, the spasing curves experience a bifurcation behavior. This is clearly seen in the magnified plot in Figure 3B; there is the threshold at the bifurcation point and two branches of the spasing curve above it. As we see from Figure 3C, these two branches differ by the stationary values of population inversion n_K; for the upper branch, it is significantly lower than for the lower branch. To answer the question whether these two branches are stable, we slightly perturb the accurate numerical solutions at $g = 25$ ps^{-1} by changing the number of SPs by a minuscule amount, $\Delta N_m = 0.0001$. The density matrix solution for the dynamics of the SP population induced by such a perturbation is shown in Figure 3D. As we see, the upper branch is absolutely stable, but the lower branch is unstable, and it evolves in time toward the upper branch within less than half a picosecond. As a result of this bifurcation instability, the system actually evolves with the increase of pumping along a path indicated by arrows in Figure 3B: Below the threshold, the population of the coherent SPs $N_m = 0$; it jumps to the apex of the curve at the bifurcation point and then follows the upper branch. One can state that the spatial inhomogeneity of the field and the inversion cause the spasing transition to become the first order. This is in contrast to the previous homogeneous case of Stockman, where this transition was continuous, i.e. of the second order.

The chiral optical fields generated by the topological spaser are not stationary – they evolve in time rotating clockwise for $m = 1$, as illustrated in Figure 4, and counterclockwise for $m = -1$. The magnitude of the field is large even for one SP per mode, $|\mathbf{E}| \sim 10^7$ V/Å, which is a general property of the nanospasers related to the nanoscopic size of the mode. Note that with increase of the SP population the field increases as $|\mathbf{E}| \propto \sqrt{N_m}$.

3.3 Stability and topological protection of spaser modes

In Figure 5A, we test the stability and topological protection of the spasing mode. Figure 5A displays the dynamics of the SP population of the topological spaser, $N_m(t)$, for different initial numbers of SPs, $N_m(0)$, and for their different chiralities, $m = \pm 1$. As these data show, the left-rotating SPs ($m = -1$) are not amplified irrespective of their initial numbers; the corresponding curves evolve with decaying relaxation oscillations tending to $N_{-1} = 0$. In contrast, the $m = 1$ SPs exhibit a stable amplification; their number increases to a level that is defined by the pumping rate, g, and does not depend on the initial populations.

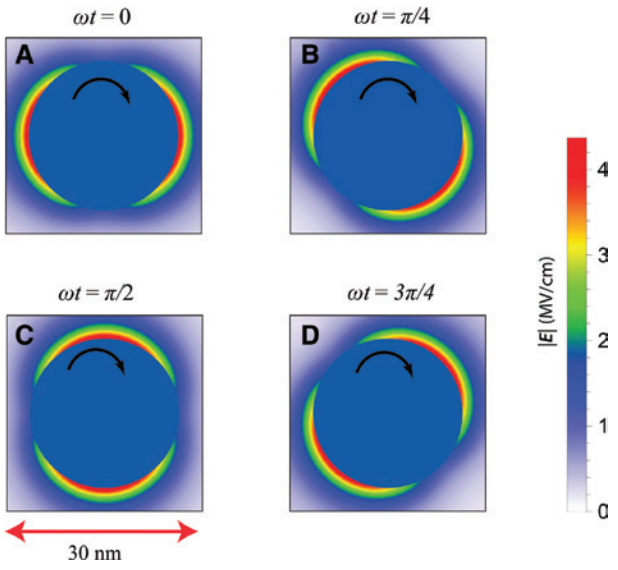

Figure 4: Temporal dynamics of the local electric field, $|\mathbf{E}|$, in topological spaser generating in the $m = 1$ mode.
The curved arrow indicates the rotation direction of the field (clockwise). The magnitude of the field is calculated for a single SP per mode, $N_m = 1$; it is color coded by the bar to the right. The phase of the spaser oscillation is indicated at the top of the corresponding panels.

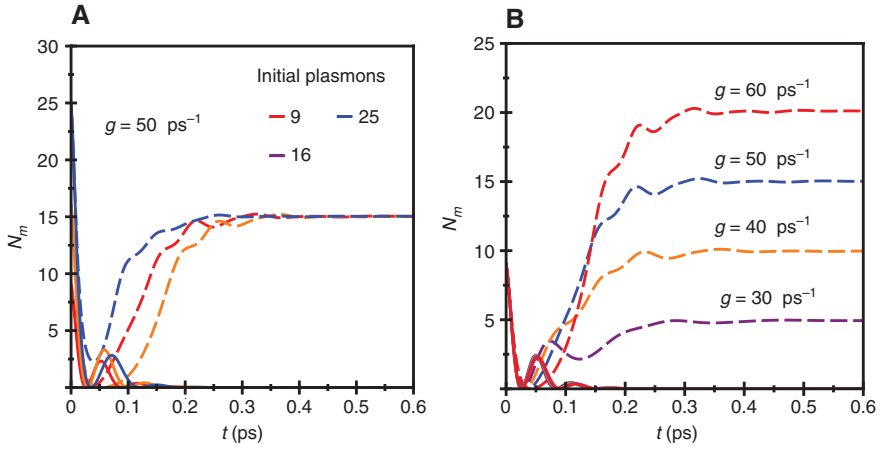

Figure 5: Number of SPs, N_m, as a function of time t for a spaser with MoS_2 as a gain material.
The pumping is performed by a radiation whose electric field rotates clockwise in the plane of system ($m=1$). The solid lines denote the chiral SPs with $m=-1$, and the dashed lines denote the SPs with $m=1$. The pumping rates are indicated in the panels. (A) Dependence of SP number, N_m, on time t after the beginning of the pumping for different initial SP populations (color coded as indicated) for pumping rate $g=50$ ps^{-1}. (B) Dependence of SP number N_m on time t for different pumping rates g (color coded). The initial SP number is $N_m=10$.

The chirality of the generating (spasing) SP mode is always a clean $m=1$ (in this case) or $m=-1$ for the K' valley pumping. It is determined by the underlying chirality of the electron states of the corresponding (K or K') valley. It is stable with respect to even nonsmall perturbations; the injected $m=-1$ SPs are not amplified and decay to zero because the corresponding mode is below the spasing threshold. Despite the fact that the underlying chiral electronic state of the K valley does not have a perfectly quantized topological charge, the spasing SP mode does; it is a pure $m=1$ (or, $m=-1$) chiral state, which corresponds to a conserved topological charge of ±1. This "purification" of the state is due to the highly nonlinear, threshold nature of the spaser amplification. This stable topological charge $m=1$ (or, $m=-1$) of the spasing mode is determined by the sign of the underlying Berry curvature of the valley electron states, and its conservation and stability with respect to perturbations can be interpreted as topological protection.

As a complementary test, we show in Figure 5B the temporal dynamics of the SP population for equal initial number of SPs but different pumping rates. The dynamics in this case is again stable with the mismatched $m=-1$ SPs decaying to zero and the matched $m=1$ being amplified to the stable levels that linearly increase with the pumping rate.

3.4 Far-field radiation of spaser

The spaser is a subwavelength device design to generate intense, coherent nanolocalized fields. Generation of far-field radiation is not its primary function. However, the proposed spaser, as most existing nanospasers, generates in a dipolar mode that will emit in the far field. This emission, in absolute terms, can be quite intense for a nanosource. In particular, the spaser emission was used to detect cancer cells in the blood flow model [16]; it was, actually, many orders of magnitude brighter than from any other label for biomedical detection.

To describe the spaser emission, we note that the radiating dipole uniformly rotates with the angular velocity of ω_{sp}. The emitted radiation will be right-hand circularly polarized for the pumping at the K point and left-hand circularly polarized for the K' pumping. Note that the corresponding two radiating modes are completely uncoupled. This is equivalent to having two independent chiral spasers in one.

To find the intensity, I, of the emitted radiation, we need to calculate the radiating dipole. To do so, we will follow Stockman [45]. We take into account that the modal field, $\mathbf{E}_m=\nabla\phi_m$, inside the metal spheroid is constant. Then from (32) in see Supplementary Materials, we can find

$$E_m^2=\frac{s_{sp}}{V_m}, \tag{20}$$

where V_m is the spheroid's volume. The physical field squared inside the metal is found from (3) and (4),

$$F_m^2=\frac{4\pi\hbar s_{sp}^2 N_m}{\varepsilon_d s_{sp}' V_m}. \tag{21}$$

From this, we find the radiating dipole squared as

$$\left|d_{0p}\right|^2 = \frac{\hbar}{4\pi}\left(\mathrm{Re}\frac{\partial\varepsilon_m(\omega_{sp})}{\partial\omega_{sp}}\right)^{-1}\mathrm{Re}[\varepsilon_m(\omega_{sp})-\varepsilon_d]^2 V_m N_m\,. \quad (22)$$

The dipole radiation rate (photons per second) can be found from a standard dipole-radiation formula [46] as

$$I = \frac{4}{9}\left(\frac{\omega}{c_0}\right)^3(\varepsilon_d)^{1/2}\mathrm{Re}[\varepsilon_m(\omega_{sp})-\varepsilon_d]^2\times\left(\mathrm{Re}\frac{\partial\varepsilon_m(\omega_{sp})}{\partial\omega_{sp}}\right)^{-1} a^2 c N_m\,, \quad (23)$$

where c_0 is speed of light in vacuum.

For our example of MoS_2, substituting parameters that we used everywhere in our calculations (see *Parameters of spaser and chiral coupling to gain medium*), we obtain

$$I = 2.1\times10^{12} N_m\ \mathrm{s}^{-1};\ \ P = \hbar\omega_{sp} I = 0.55\ N_m\ \mu\mathrm{W}\,, \quad (24)$$

where P is the power of the emission. From these numbers, we conclude that the emission is extremely bright for a nanoemitter and easily detectable. This is in line with the observation of the emission from single spasers of the comparable size in Galanzha et al. [16].

4 Concluding discussion

In this article, we introduce a topological nanospaser that consists of a plasmonic metal spheroid as the SP resonator and a nanoflake of a semiconductor TMDC as the gain medium. This spaser has two mutually $\mathcal{T}$-reversed dipole modes with identical frequencies but opposite chiralities (topological charges $m=\pm1$). Only the mode whose chirality matches that of the active (pumped) valley, i.e. $m=1$ for the K valley and $m=-1$ for the K' valley, can be generated while the conjugated mode does not go into generation at any pumping level. The topological spaser is stable with respect to even large perturbations: the SP with mismatched topological charge injected into the system even in large numbers decay exponentially within a ~100-fs time. This implies a strong topological protection.

This protection is not trivial because the exact valley selection rule matching its chirality to that of the SPs is strictly valid only on the symmetry axis of the metal spheroid (in the center of the TMDC gain-medium flake). Off-axis, there is a coupling of the gain to the chirally mismatched SPs. However, the strong topological protection appears because of the fact that the spaser is a highly nonlinear, threshold phenomenon. In fact, it is the nonlinear saturation of the gain and the concurrent clamping of the inversion that cause the strong mode competition. The topologically matched mode ($m=1$ for the K valley and $m=-1$ for the K' valley) reaches the threshold first and saturates the gain, thus preventing the mismatched mode from the generation under any pumping or any perturbations.

The chiral selectivity of the topological nanospaser stems from the valley-selective pumping of the gain-medium TMDC. The direct intervalley scattering of carriers, which would compromise such a selectivity, is a low-probability process due to the very large required crystal momentum transfer and can be safely neglected. However, there is another process related to a long-range exciton exchange interaction (EEI) that can induce valley polarization decay [47–49]. This long-range-EEI valley polarization decay can potentially compromise the valley-specific pumping and population inversion and affect the topological spasing process. However, the valley polarization decay induced by the EEI is relatively slow; it occurs with a characteristic time of $\tau_{EEI}\sim4$–7 ps. This process appears to be too slow to affect the spasing because the characteristic relaxation times for the spaser are much shorter due, in part, to the plasmonic enhancement of the relaxation by the metal. A typical spontaneous decay time of the upper spasing level of the gain medium calculated from (17) is estimated to be $\tau_2\approx250$ fs. This time is an order of magnitude shorter than τ_{EEI}; note that the corresponding stimulated decay time is typically yet another order of magnitude shorter. This renders the EEI to be orders of magnitude too slow to compete with the functioning of the topological spaser.

The proposed topological spaser is promising for use in nano-optics and nanospectroscopy where strong rotating nanolocalized fields are required. It may be especially useful in applications to biomolecules and biological objects, which are typically chiral. It may also be used as a nanosource of a circularly polarized radiation in the far field, in particular, as a biomedical multifunctional agent similar to the use of spherical spasers in the study of Galanzha et al. [16].

Acknowledgment: Major funding was provided by the Materials Sciences and Engineering Division of the Office of the Basic Energy Sciences, Office of Science, U.S. Department of Energy (grant no. DE-SC0007043). Numerical simulations have been performed using support by the Chemical Sciences, Biosciences and Geosciences Division, Office of Basic Energy Sciences, Office of Science, US Department of Energy (grant no. DE-FG02-01ER15213). The work of V.A. was supported by NSF EFRI NewLAW (grant EFMA-17 41691). Support for J.-S.W. came

from MURI (grant no. N00014-17-1-2588, Funder Id: http://dx.doi.org/10.13039/100000006) from the Office of Naval Research (ONR).

References

[1] Li K, Li X, Stockman MI, Bergman DJ. Surface plasmon amplification by stimulated emission in nanolenses. Phys Rev B 2005;71:115409.

[2] Fedyanin DY. Toward an electrically pumped spaser. Opt Lett 2012;37:404–6.

[3] Baranov DG, Vinogradov AP, Lisyansky AA, Strelniker YM, Bergman DJ. Magneto-optical spaser. Opt Lett 2013;38:2002–4.

[4] Zheludev NI, Prosvirnin SL, Papasimakis N, Fedotov VA. Lasing spaser. Nat Phot 2008;2:351–4.

[5] Noginov MA, Zhu G, Belgrave AM, et al. Wiesner. Demonstration of a spaser-based nanolaser. Nature 2009;460:1110–2.

[6] Oulton RF, Sorger VJ, Zentgraf T, et al. Plasmon lasers at deep subwavelength scale. Nature 2009;461:629–32.

[7] Ma RM, Oulton RF, Sorger VJ, Bartal G, Zhang X. Room-temperature sub-diffraction-limited plasmon laser by total internal reflection. Nat Mater 2011;10:110–3.

[8] Flynn RA, Kim CS, Vurgaftman I, et al. A room-temperature semiconductor spaser operating near 1.5 micron. Opt Express 2011;19:8954–61.

[9] Marell MJH, Smalbrugge B, Geluk EJ, et al. Plasmonic distributed feedback lasers at telecommunications wavelengths. Opt Express 2011;19:15109–18.

[10] van Beijnum F, van Veldhoven PJ, Geluk EJ, Dood MJA, Hooft GW, van Exter MP. Surface plasmon lasing observed in metal hole arrays. Phys Rev Lett 2013;110:206802.

[11] Lu YJ, Wang CY, Kim J, et al. All-color plasmonic nanolasers with ultralow thresholds: autotuning mechanism for single-mode lasing. Nano Lett 2014;14:4381–8.

[12] Zhang Q, Li G, Liu X, et al. A room temperature low-threshold ultraviolet plasmonic nanolaser. Nat Commun 2014;5:4953.

[13] Chou BT, Chou YH, Wu YM, et al. Single-crystalline aluminum film for ultraviolet plasmonic nanolasers. Sci Rep 2016;6:19887.

[14] Lee CJ, Yeh H, Cheng F, et al. Low-threshold plasmonic lasers on a single-crystalline epitaxial silver platform at telecom wavelength. ACS Photonics 2017;4:1431–9.

[15] Sun S, Zhang C, Wang K, Wang S, Xiao S, Song Q. Lead halide perovskite nanoribbon based uniform nanolaser array on plasmonic grating. ACS Photonics 2017;4:649–56.

[16] Galanzha EI, Weingold R, Nedosekin DA, et al. Spaser as a biological probe. Nat Commun 2017;8:15528–1–7.

[17] Ma R, Yin X, Oulton RF, Sorger VJ, Zhang X. Multiplexed and electrically modulated plasmon laser circuit. Nano Lett 2012;12:5396–402.

[18] Ma RM, Ota S, Li Y, Yang S, Zhang. Explosives detection in a lasing plasmon nanocavity. Nat Nanotechnol 2014;9:600–4.

[19] Wang S, Li B, Wang XY, et al. High-yield plasmonic nanolasers with superior stability for sensing in aqueous solution. ACS Photonics 2017;4:1355–60.

[20] Wu Z, Chen J, Mi Y, et al. All-inorganic $CsPbBr_3$ nanowire based plasmonic lasers. Adv Opt Mater 2018;6:1800674.

[21] Lu Y-J, Kim J, Chen H-Y, et al. Plasmonic nanolaser using epitaxially grown silver film. Science 2012;337:450–3.

[22] Gwo S, Shih C-K. Semiconductor plasmonic nanolasers: current status and perspectives. Rep Prog Phys 2016;79:086501.

[23] Ning C-Z. Semiconductor nanolasers and the size-energy-efficiency challenge: a review. Adv Photonics 2019;1:014002.

[24] Kress SJP, Cui J, Rohner P, et al. A customizable class of colloidal-quantum-dot spasers and plasmonic amplifiers. Sci Adv 2017;3:e1700688.

[25] Plum E, Fedotov VA, Kuo P, Tsai DP, Zheludev NI. Towards the lasing spaser: controlling metamaterial optical response with semiconductor quantum dots. Opt Express 2009;17:8548–51.

[26] Huang Y-W, Chen WT, Wu PC, Fedotov VA, Zheludev NI, Tsai DP. Toroidal lasing spaser. Sci Rep 2013;3:1237.

[27] Zhou W, Dridi M, Suh JY, et al. Lasing action in strongly coupled plasmonic nanocavity arrays. Nat Nano 2013;8:506–11.

[28] Wu J-S, Apalkov V, Stockman MI. Topological spaser. Phys Rev Lett 2020;124:017701.

[29] Wang XY, Wang YL, Wang S, et al. Lasing enhanced surface plasmon resonance sensing. Nanophotonics 2017;6:472–8.

[30] Stockman M. Spasers to speed up CMOS processors, USA Patent No. 10,096,675.

[31] Berry MV. Quantal phase factors accompanying adiabatic changes. Proc R Soc Lond Ser A 1984;392:45–57.

[32] Xiao D, Chang M-C, Niu Q. Berry phase effects on electronic properties. Rev Mod Phys 2010;82:1959–2007.

[33] You YM, Zhang XX, Berkelbach TC, Hybertsen MS, Reichman DR, Heinz TF. Observation of biexcitons in monolayer WSe2. Nat Phys 2015;11:477–82.

[34] Novoselov KS, Mishchenko A, Carvalho A, Neto AHC. 2D materials and van der Waals heterostructures. Science 2016;353:461.

[35] Basov DN, Fogler MM, de Abajo FJG. Polaritons in van der Waals materials. Science 2016;354:195.

[36] Salehzadeh O, Djavid M, Tran NH, Shih I, Mi Z. Optically pumped two-dimensional mos2 lasers operating at room-temperature. Nano Lett 2015;15:5302–6.

[37] Ye Y, Wong ZJ, Lu X, et al. Monolayer excitonic laser. Nat Phot 2015;9:733–7.

[38] Wu S, Buckley S, Schaibley JR, et al. Monolayer semiconductor nanocavity lasers with ultralow thresholds. Nature 2015;520:69–72.

[39] Cao T, Wang G, Han W, et al. Valley-selective circular dichroism of monolayer molybdenum disulphide. Nat Commun 2012;3:887.

[40] Ye Z, Sun D, Heinz TF. Optical manipulation of valley pseudospin. Nat Phys 2016;13:26–30.

[41] Wu S, Buckley S, Schaibley JR, et al. Monolayer semiconductor nanocavity lasers with ultralow thresholds. Nature 2015;520:69–72.

[42] Bloch F, Siegert A. Magnetic resonance for nonrotating fields. Phys Rev 1940;57:522–7.

[43] Agarwal GS. Rotating-wave approximation and spontaneous emission. Phys Rev A 1971;4:1778–81.

[44] Liu GB, Shan WY, Yao YG, Yao W, Xiao D. Three-band tight-binding model for monolayers of group-VIB transition metal dichalcogenides. Phys Rev B 2013;88:085433.

[45] Stockman MI. Nanoplasmonics: past, present, and glimpse into future. Opt Express 2011;19:22029–106.

[46] Landau LD, Lifshitz EM. The classical theory of fields. Oxford, NY: Pergamon Press; 1975.
[47] Glazov MM, Amand T, Marie X, Lagarde D, Bouet L, Urbaszek B. Exciton fine structure and spin decoherence in monolayers of transition metal dichalcogenides. Phys Rev B 2014;89:201302.
[48] Zhu CR, Zhang K, Glazov M, et al. Exciton valley dynamics probed by Kerr rotation in wse_2 monolayers. Phys Rev B 2014;90:161302.
[49] Wang G, Chernikov A, Glazov MM, et al. Colloquium: excitons in atomically thin transition metal dichalcogenides. Rev Mod Phys 2018;90:021001.

Supplementary Material: The online version of this article offers supplementary material (https://doi.org/10.1515/nanoph-2019-0496).